



Article

Structural and Optical Properties of Tungsten Disulfide Nanoscale Films Grown by Sulfurization from W and WO₃

Pangihutan Gultom¹, Jiang-Yan Chiang¹, Tzu-Tai Huang¹, Jung-Chuan Lee¹, Shu-Hsuan Su¹ 
and Jung-Chung Andrew Huang^{1,2,3,*}

¹ Department of Physics, National Cheng Kung University, Tainan 701, Taiwan; pangihutangultom36@gmail.com (P.G.); b36355602@gmail.com (J.-Y.C.); asd4561377@gmail.com (T.-T.H.); leejungchuan@gmail.com (J.-C.L.); macg0510@yahoo.com.tw (S.-H.S.)

² Department of Applied Physics, National University of Kaohsiung, Kaohsiung 811, Taiwan

³ Taiwan Consortium of Emergent Crystalline Materials, Ministry of Science and Technology, Taipei 10601, Taiwan

* Correspondence: jcahuang@mail.ncku.edu.tw; Tel.: +886-6-2757575

Abstract: Tungsten disulfide (WS₂) was prepared from W metal and WO₃ by ion beam sputtering and sulfurization in a different number of layers, including monolayer, bilayer, six-layer, and nine-layer. To obtain better crystallinity, the nine-layer of WS₂ was also prepared from W metal and sulfurized in a furnace at different temperatures (800, 850, 900, and 950 °C). X-ray diffraction revealed that WS₂ has a 2-H crystal structure and the crystallinity improved with increasing sulfurization temperature, while the crystallinity of WS₂ sulfurized from WO₃ (WS₂-WO₃) is better than that sulfurized from W-metal (WS₂-W). Raman spectra show that the full-width at half maximum (FWHM) of WS₂-WO₃ is narrower than that of WS₂-W. We demonstrate that high-quality monocrystalline WS₂ thin films can be prepared at wafer scale by sulfurization of WO₃. The photoluminescence of the WS₂ monolayer is strongly enhanced and centered at 1.98 eV. The transmittance of the WS₂ monolayer exceeds 80%, and the measured band gap is 1.9 eV, as shown by ultraviolet-visible-infrared spectroscopy.

Keywords: WS₂; ion beam sputtering technique; W-metal and WO₃ sulfurization; monolayer crystal structure; optical properties



Citation: Gultom, P.; Chiang, J.-Y.; Huang, T.-T.; Lee, J.-C.; Su, S.-H.; Huang, J.-C.A. Structural and Optical Properties of Tungsten Disulfide Nanoscale Films Grown by Sulfurization from W and WO₃. *Nanomaterials* **2023**, *13*, 1276. <https://doi.org/10.3390/nano13071276>

Academic Editors: Josefina Pons and Tsuyoshi Asahi

Received: 20 February 2023

Revised: 28 March 2023

Accepted: 31 March 2023

Published: 4 April 2023



Copyright: © 2023 by the authors. Licensee MDPI, Basel, Switzerland. This article is an open access article distributed under the terms and conditions of the Creative Commons Attribution (CC BY) license (<https://creativecommons.org/licenses/by/4.0/>).

1. Introduction

Tungsten disulfide (WS₂) is a two-dimensional (2-D) material consisting of a covalently bonded sheet of W atoms filled between two trigonal sheets of S atoms. WS₂ is mainly composed of three structures, hexagonal (2-H), trigonal (1T), or rhombohedral (3R) phase. Among them, the 2H phase structure is relatively stable and exhibits better optical properties [1]. The interlayers of WS₂ are bound only by weak van der Waals forces, and the interlayer spacing is ~0.6 nm [2,3].

WS₂ has been extensively studied due to its unique layer-dependent properties, such as the ability to absorb 5–10% of incident sunlight [4], and its unique band structure. Monolayer WS₂ exhibits a direct band gap [5] of 1.98 eV [6], while multilayer WS₂ shows an indirect band gap [7] of about 1.3 eV [8,9]. This phenomenon can be attributed to the lack of Coulomb repulsion between the p_z orbitals of the chalcogenide elements in adjacent layers, leading to stabilization of the Γ -state valence band [10]. WS₂ has been investigated for applications such as solar cells [11], hydrogen evolution reactions (HER) [12], electrocatalysis [13], batteries [14], and transistors [15]. However, the efficiency of most of the devices remains low. Therefore, a better understanding of the formation and physical properties of WS₂ is essential. Many efforts have been made to improve the application value of WS₂, such as controlling the formation mechanism, including studying the growth mode of the films to obtain a uniform, large-area [16], and well-oriented crystals. There are three common methods for depositing WS₂ thin films: the stripping method [17], the chemical vapor

deposition (CVD) [18,19], and the direct vulcanization synthesis method [20]. In this study, we seek to obtain high-quality WS₂ films by comparing tungsten (W) metal and oxide (WO₃) sulfurization processes. The structural and optical properties of the WS₂ thin films were investigated in detail for future applications in next-generation optoelectronic devices.

2. Experimental

The W and WO₃ films were prepared on c-axis Al₂O₃ (1 cm², provided by Bangjie Material Technology). First, the Al₂O₃ substrate was ultrasonicated in acetone for 5 min to remove dirt and then rinsed with methanol. The cleaned c-axis sapphire was then inserted into the ion beam sputtering (IBS, Commonwealth Scientific) chamber for the growth of W or WO₃ films. Subsequently, the grown W or WO₃ films were sulfurized to obtain WS₂ films, as schematically shown in Figure S1a,b of the Supplementary Document. The sputtering of W films was performed at a base pressure of about 5×10^{-6} Torr. Ar (99.999% purity) was introduced into the chamber at a flow rate of 5 sccm to initiate sputtering process. On the other hand, the WO₃ films were grown by flowing Ar and oxygen at flow rates of 5 and 3 sccm, respectively. The sulfurization of the W and WO₃ films was carried out in a horizontal quartz-tube furnace. The W or WO₃ films were placed in the center of the quartz-tube furnace while about 3 g of sulfur (99.999% purity) was placed next to the tube lid. The tube was then evacuated to 5×10^{-2} Torr. During the sulfurization process, nitrogen gas (99.999%) flowed into the chamber while maintaining a pressure of 0.7 Torr. In this work, the sulfurization process is maintained at 900 °C for thickness-dependent studies. To study the crystallinity behavior, the nine-layer sample of WS₂-W was sulfurized at different temperatures of 800, 850, 900, and 950 °C. All sulfurization processes were carried out for 20–30 min and cooled naturally to room temperature. The elemental compositions of the WS₂ films were examined using X-ray photoelectron spectroscopy (XPS, Thermo Fisher Scientific with an Al K α light source). The binding energies were referenced to the NIST-XPS database. The WS₂ phase was identified by micro-Raman (Horiba Jobin Yvon Lab RAM HR) equipped with an 1800-cycle grating, an objective lens with 100 \times magnification, and a laser wavelength of 532 nm. X-ray absorption near-edge spectroscopy (XANES) was performed to identify the local electron structure of WS₂. The XANES was performed at the 07A1 beamline of the National Synchrotron Radiation Research Center (Hsinchu, Taiwan). The crystal structure of WS₂ films was examined by X-ray diffraction (XRD, D8 by Bruker AXS GmbH) equipped with a Cu 2 keV light source. A high-resolution transmission electron microscope (HR-TEM, JEOL JEM-2100F CS STEM) equipped with a dual-beam focus ion beam was conducted to study the microstructure and thickness at the atomic scale. The electrons were accelerated at 12 kV and a magnification of 500 K. The TEM was also equipped with an energy-dispersive X-ray spectrometer (EDS). Further analysis was performed using micro-photoluminescence spectroscopy (PL) to study the band gap of WS₂ and ultraviolet-visible-infrared spectroscopy to understand the light absorption properties of the samples.

3. Results and Discussion

3.1. Structural Analysis

Figure 1a,b shows the XRD of WS₂-W at different sputtering thicknesses and sulfurization temperatures. All the XRD peaks marked with an asterisk match the substrate Al₂O₃ peaks. The presence of lattice planes (002), (004), (006), and (008) suggests that the structure of WS₂ is a 2H (hexagonal) phase [5]. Moreover, the interlayer spacing of the WS₂ was estimated to be ~0.62 nm using the Bragg equation, which agrees with the theory and previous results [21,22].

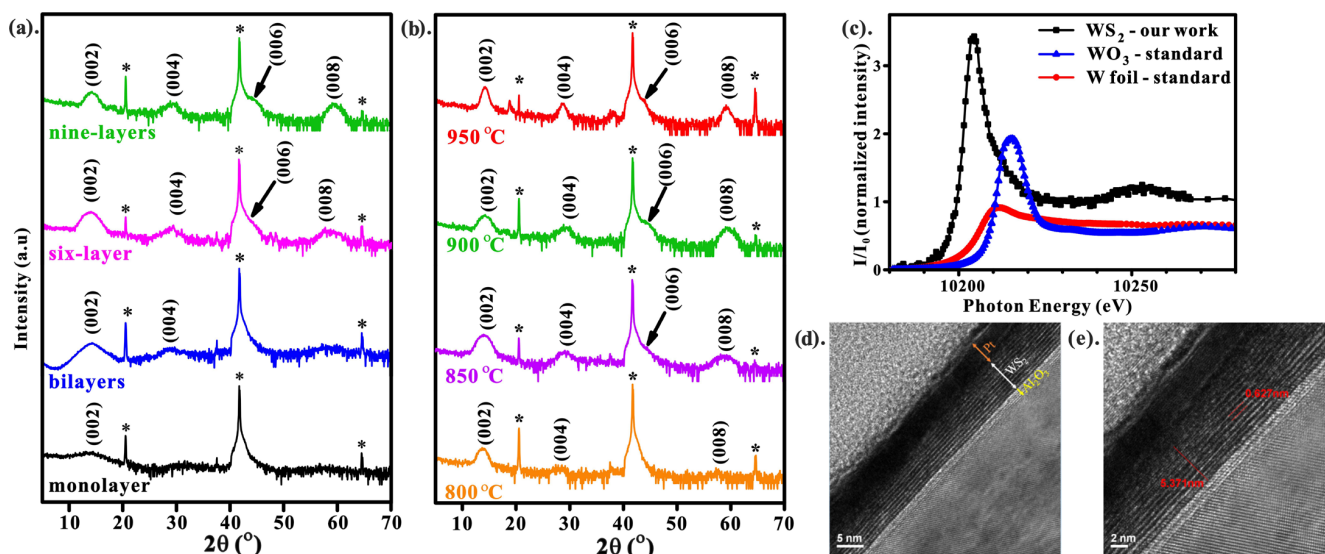


Figure 1. Structure and morphology of WS₂. The XRD spectra of WS₂ films for (a) different numbers of layers; (b) different sulfurization temperatures of nine-layer of WS₂; (c) the morphology of the WS₂ is presented by TEM image; (d) the HR-TEM shows the interlayer distance of WS₂ stacking layer; (e) the XANES shows the local structure of WS₂.

With increasing film thickness, the intensity of XRD signals (002), (004), (006), and (008) increases, while the FWHM of each peak is reduced, as shown in Figure 1a, indicating that the crystallinity of the films improves with the number of WS₂ layers. The absence of the (002) peak for the monolayer of WS₂ is due to the diffraction limit. The tungsten films were sulfurized at different temperatures of 800, 850, 900, and 950 °C to obtain the optimum temperature for formation WS₂ (nine-layer sample). The corresponding XRD results are shown in Figure 1b, indicating that the crystallinity of WS₂ improves with increasing sulfurization temperature. Additionally, to study the local structure of WS₂, the X-ray absorption near-edge structure (XANES) was also performed at W L₃-edge. Figure 1c exhibits the spectrum of WS₂ with tungsten and tungsten trioxide as references. The XANES of WS₂ agrees with the previous result [23]. In addition, it also confirms that the WS₂ (black path) has a 2H (hexagonal) structure.

TEM investigation has been carried out to observe the atomic stacking of WS₂ (nine-layer sample). In order to improve the conductivity of the film, about 5 nm of platinum was deposited on the surface of WS₂. Platinum was also used to protect the sample from oxidation. Figure 1c shows the TEM image of the nine-layer of WS₂ stacked along the c-axis with the platinum capping layer. The total thickness of the WS₂ layer was estimated to be ~5.37 nm with an interplanar spacing of 0.62 nm (Figure 1d), which agrees with the XRD result.

3.2. Elemental Composition Analysis

The elemental composition of WS₂ was qualitatively examined by X-ray photoelectron spectroscopy (XPS). Figure 2 shows high-resolution XPS spectra in W⁴⁺ and S²⁻ energy regions. Figure 2a exhibits the tungsten signals at 32.6, 34.8, and 38.2 eV, which can be ascribed to W 4f_{7/2}, W 4f_{5/2}, and W 5f_{3/2}, respectively, with a spin-orbit splitting of ΔE_p (4f_{7/2} – 4f_{5/2}) = 2.2 eV. The existence of high-intensity signals at 32.6 and 34.8 eV also suggests the formation of 2H-WS₂, which concurs with previous reports [24,25]. Figure 2b shows the spectrum of the doublet S 2p at 163.5 eV and 162.3 eV, representing S 2p_{1/2} and S 2p_{3/2}, respectively [26,27]. These peaks are attributed to the divalent sulfide ions (S²⁻), which are also associated with the formation of 2H-WS₂. The elemental composition of WS₂ was estimated to be 56.0, 28.7, and 15.3% (in atomic percentage) for S 2p, W 4f, and O 1s, in order. The oxygen signal is from the sapphire substrate. Therefore, the W and S ratio

is very close to 2:1, confirming that the samples are in good stoichiometry. Additionally, the elemental composition of WS_2 was also qualitatively examined using EDS (Figure S2).

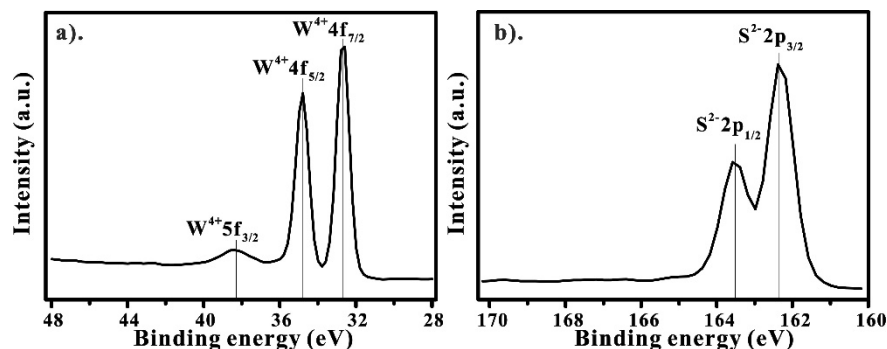


Figure 2. High-resolution XPS of WS_2 films: (a) W 4f and W 5f signals; (b) S 2p.

3.3. Optical Properties

3.3.1. Micro-PL Spectroscopy

Micro-PL has been performed to study the optical and electronic properties of WS_2 . It is found that the PL signal comes from the energy gap of the direct transition when the thickness is reduced below two atomic layers. The PL of WS_2 is strongly suppressed as thickness increases above two atomic layers, in which the indirect band gap is completely formed.

Figure 3 shows the PL peaks of the monolayer and bilayer of WS_2 . The peaks are centered at 1.98 and 1.95 eV, respectively, in good agreement with previous results (2.1–1.9 eV) [28] and with the DFT-LDA calculations for the monolayer and the bilayer of WS_2 [29,30]. The PL intensity shows a slight redshift (~ 3 eV) and a threefold decrease in intensity as the layer increases from the monolayer to the bilayer of WS_2 [3]. The peak shift is likely due to the proportional relationship between layer number and carrier concentration, which also contributes to Coulomb scattering [31]. This result is in line with the theoretical prediction that the WS_2 monolayer has a direct band gap at the Γ point [32].

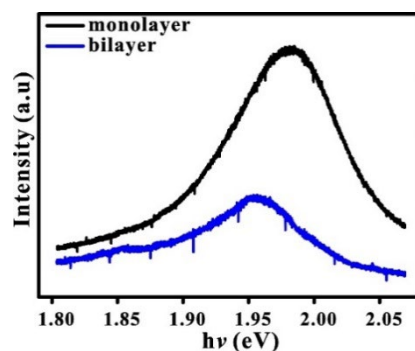


Figure 3. Photoluminescence spectra of WS_2 monolayer and bilayer.

3.3.2. Ultraviolet-Visible-Infrared Spectroscopy

The optical properties of WS_2 were further investigated using an ultraviolet-visible-infrared (UV/visible/NIR) spectrophotometer, as shown in Figure 4. It was observed that the transmittance of WS_2 increased from 40% (nine-layer) to over 80% (monolayer) in the UV-visible region (Figure 4a). The band gap of the WS_2 monolayer is about 1.9 eV, as estimated from the Tauc plot of the absorption spectrum (Figure 4b).

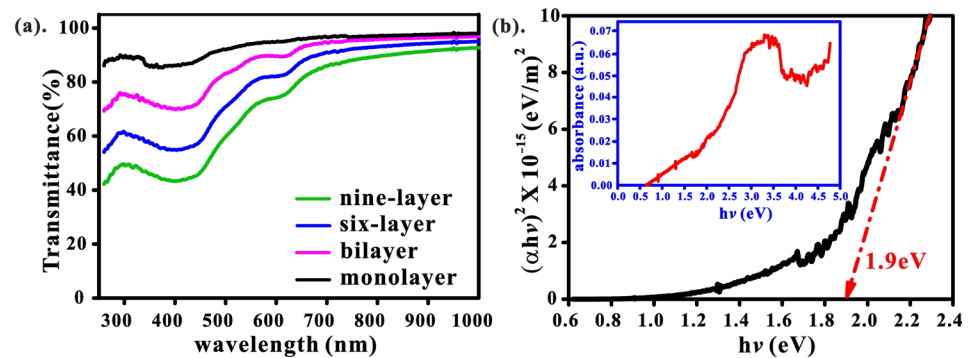


Figure 4. (a) Comparison of the transmittance of the WS₂ thin film with different thicknesses; (b) Tauc diagram of monolayer WS₂ from the absorption. Inset: the absorption measurement can be used to determine the band gap of WS₂.

3.4. Comparison of WS₂-W and WS₂-WO₃

3.4.1. XRD of WS₂-W and WS₂-WO₃

In order to obtain high-quality WS₂ films, we compared the sulfurization of W and WO₃ films, termed as WS₂-W and WS₂-WO₃, respectively. The samples were sulfurized side by side at 900 °C. The XRD results are shown in Figure 5. It was revealed that the diffraction peaks of WS₂-WO₃ are sharper and narrower than those of WS₂-W with similar thickness, suggesting that the crystallinity of WS₂-WO₃ is better than that of WS₂-W.

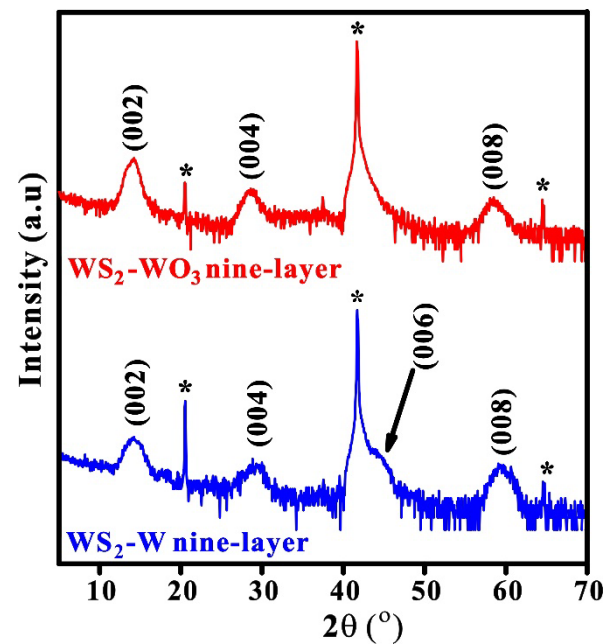


Figure 5. XRD of nine-layer WS₂ sulfurized from W and WO₃ at 900 °C It shows narrower FWHMs of 002, 004, and 008 signals from WS₂-WO₃ (2.1 ± 0.1 ; 3.4 ± 0.2 ; 2.6 ± 0.2 , respectively) than from WS₂-W (2.2 ± 0.1 ; 4.1 ± 0.2 ; 3.1 ± 0.2 , respectively).

3.4.2. Raman Spectra of WS₂-W and WS₂-WO₃

Raman spectroscopy is widely used for elemental analysis, layer stacking order, and doping effect of transition metal dichalcogenides [33]. Figure 6 shows the Raman spectra of WS₂-W and WS₂-WO₃ with the different number of stacked layers.

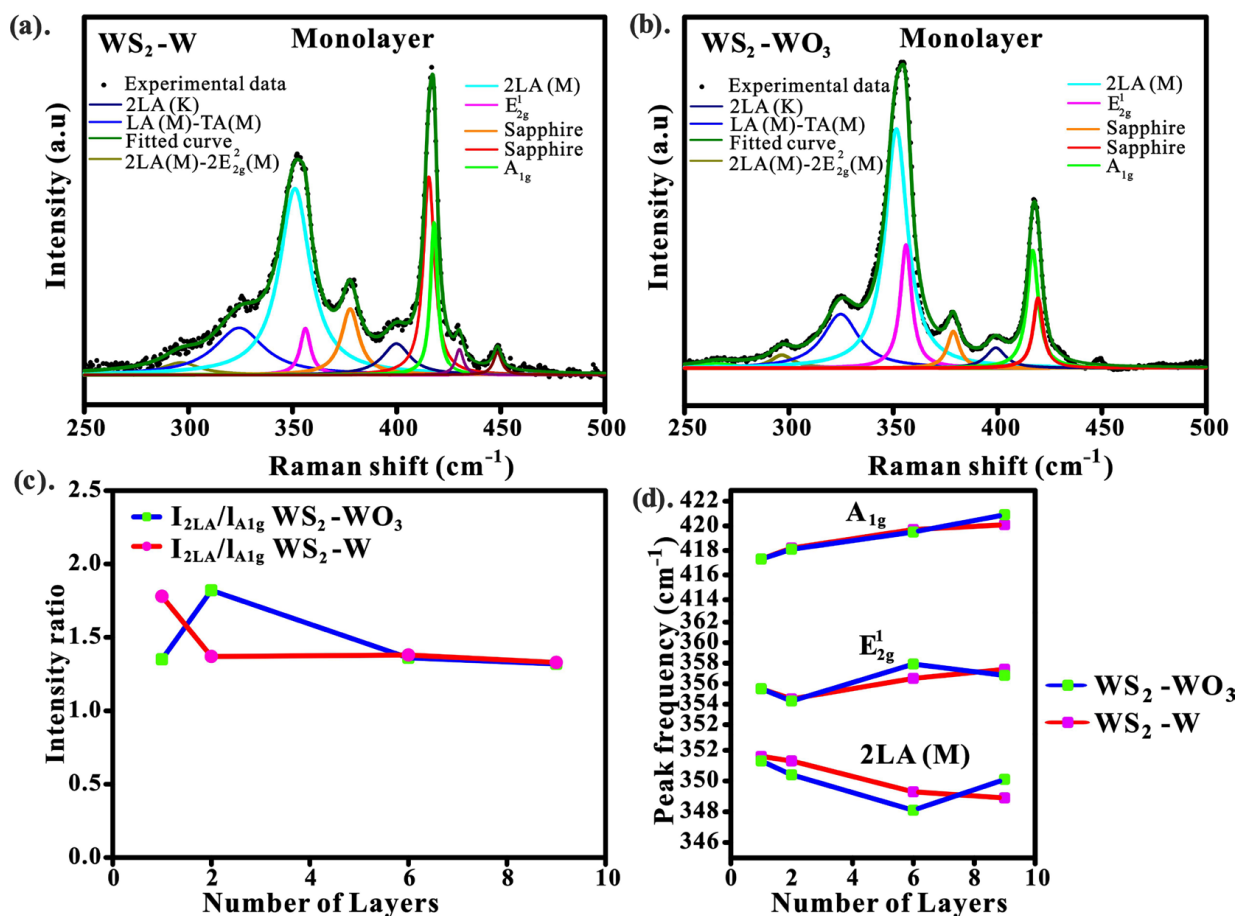


Figure 6. (a,b). Deconvolution of the Raman spectra of WS₂-W and WS₂-WO₃, respectively, using Lorentz fitting method; (c) the intensity ratio of $I_{2LA}/I_{A_{1g}}$ as a function of the number layers of WS₂; (d) the peak positions of A_{1g} , E_{2g}^1 , and 2LA with respect to the number layer of WS₂. Additionally, the deconvolution of the Raman spectra for bilayer, six-layer, nine-layer can be seen in the Supplementary Documents.

Figure 6a,b shows two main Raman peaks centered at ~ 354 and ~ 420 cm⁻¹, respectively. These Raman peaks agree with previous work [21,34,35]. It was observed that the A_{1g} peaks overlap with the Raman peaks of sapphire (380 and 417 cm⁻¹) [36] when the Raman peaks were deconvoluted using a multi-peak Lorentzian fitting method [37]. Deconvolution of Raman peaks also revealed three strong peaks, which are E_{2g}^1 (in-plane displacement of W and S), A_{1g} (out-plane displacement of S-S atoms), and 2LA (M) (second order Raman peak), which are centered at ~ 356 , ~ 418 , and ~ 351 cm⁻¹, respectively. Furthermore, the approximate distance between A_{1g} and E_{2g}^1 of WS₂-W is ~ 61.8 , 63.8, 61.6, and 64.1 cm⁻¹ for monolayer, bilayer, six-layer, and nine-layer samples, respectively, which is not much different from the distance for WS₂-WO₃ of about 61.8, 63.7, 63.2, 62.7 in the same order. Figure 6c shows the $I_{2LA}/I_{A_{1g}}$ intensity ratio of WS₂-W reduces from the monolayer (1.8) to the nine-layer (1.3). However, WS₂-WO₃ shows a slightly different trend, where the intensity ratio increases from the monolayer (1.3) to the bilayer (1.8), and then decreases to the nine-layer (1.3). The results suggest that the second-order Raman peak intensity (I_{2LA}) is almost twice that of the first-order $I_{A_{1g}}$. This is consistent with the previous results [38,39]. Additionally, for both WS₂-W and WS₂-WO₃ samples, as the film thickness decreases, the A_{1g} signals show a slight red shift of about ~ 2.3 cm⁻¹ (Figure 6d). The redshift of A_{1g} is likely associated with reducing the atomic restoring forces. When the number of WS₂ layers is decreased, the long-range Coulomb interaction between effective

charges and dielectric screening is enhanced, leading to increased restoring force between the S-S atoms [3].

Due to the dielectric screening effect, the Raman signal is sensitive to the interactions between atoms in the interlayer and long-range Coulomb interactions [40]. The Raman wavevector and the intensity of WS_2 are strongly correlated with the layer thickness at the nanoscale level. In this work, we also used Raman spectra to calibrate the thickness of WS_2 as a monolayer, bilayer, six-layer, and nine-layer [31,39]. The Raman spectra confirmed that WS_2 was well-formed as WS_2 -W and WS_2 - WO_3 . It is clear that the peak intensity and FWHM of E_{2g}^1 for WS_2 - WO_3 are narrower than that of WS_2 -W (Table S1 in the Supplementary Materials). The average estimation of FWHM of WS_2 - WO_3 is ~ 7.2 ; however, the WS_2 -W is ~ 10.1 , suggesting WS_2 - WO_3 has better crystallinity than WS_2 -W. This is consistent with the XRD results (Figure 5). This phenomenon can be attributed to the fact that sulfur can replace oxygen more effectively at a relatively lower temperature [41], while WS_2 formed from tungsten metal requires a higher temperature to facilitate metal–sulfur bonding [42]. As a result, the defect density in WS_2 - WO_3 is likely to be lower than in WS_2 -W.

4. Conclusions

We report a study of nanoscale WS_2 films with various number of layers, prepared by sulfurization of W and WO_3 at different temperatures (800 to 950 °C). The WS_2 films were inferred to be the 2H phase and c-axis oriented. The XRD shows that the crystal quality of the WS_2 films improved with increasing sulfurization temperature. The photoluminescence of the monolayer of WS_2 is strongly enhanced and centered at 1.98 eV. The transmittance of the monolayer WS_2 exceeds 80% and the band gap is 1.9 eV, revealed by ultraviolet-visible-infrared spectroscopy. The Raman analysis shows that the FWHM of WS_2 - WO_3 is narrower than that of WS_2 -W, indicating the structure of WS_2 - WO_3 is superior to that of WS_2 -W, which is in good agreement with the X-ray diffraction result. We conclude that a large-area, high-quality WS_2 film can be prepared by sulfurizing WO_3 . The results are promising for applications in next-generation optoelectronic devices.

Supplementary Materials: The following supporting information can be downloaded at: <https://www.mdpi.com/article/10.3390/nano13071276/s1>, Figure S1: Schematic diagram: (a). W-metal and WO_3 prepared on sapphire substrate by ion beam sputtering technique; (b). W-metal or WO_3 sulfurization process using a thermocouple-equipped furnace, the process was carried out inside a horizontal quartz tube with a diameter of 50 mm and length of 100 cm; Figure S2: shows the EDS depth analysis of the WS_2 film that was carried out with Line scan mode. The small picture in the upper left corner is the relationship between the scanning position and the ratio of each element; Figure S3: the deconvolution of Raman spectra of bilayer, six-layer, and nine-layer samples using a multi-peak Lorentz fitting to separate the A_{1g} peak from the substrate and 2LA from E_{2g}^1 . The (a–c) shows the WS_2 sulfurized from tungsten metal and (d–f) shows the WS_2 sulfurized from tungsten trioxide; Table S1: Summary of the intensity ratio of $I_{2LA}/I_{A_{1g}}$ and FWHM as a function of layer numbers.

Author Contributions: J.-Y.C. and T.-T.H.; data curation, P.G.; Investigation and writing-original draft, J.-C.L. and S.-H.S.; Visualization, J.-C.A.H.; writing-review and editing. All authors discussed the results. All authors have read and agreed to the published version of the manuscript.

Funding: We would like to acknowledge the financial support from National Science and Technology Council supported this research financially under contracts NSTC 111-2124-M-006-008 and 109-2112-M-006-019-MY3.

Data Availability Statement: All data included in this study are available upon request by contact with the corresponding author.

Acknowledgments: The authors gratefully acknowledge the use of XRD 003100, SQUID 000200 and EM 012300 of MOST 110-2731-M-006-001 belonging to the Core Facility Center of National Cheng Kung University.

Conflicts of Interest: The authors declare no conflict of interest.

References

1. Mahler, B.; Hoepfner, V.; Liao, K.; Ozin, G.A. Colloidal synthesis of 1T-WS₂ and 2H-WS₂ nanosheets: Applications for photocatalytic hydrogen evolution. *J. Am. Chem. Soc.* **2014**, *136*, 14121–14127. [[CrossRef](#)] [[PubMed](#)]
2. Li, W.; Wang, T.; Dai, X.; Wang, X.; Zhai, C.; Ma, Y.; Chang, S. Bandgap engineering different stacking WS₂ bilayer under an external electric field. *Solid State Commun.* **2016**, *225*, 32–37. [[CrossRef](#)]
3. Gutierrez, H.R.; Nestor, P.L.; Ana, L.E.; Ayse, B.; Bei, W.; Ruitao, L.; Florentino, L.U.; Vincent, H.C.; Humberto, T.; Mauricio, T. Extraordinary room-temperature photoluminescence in triangular WS₂ monolayers. *Nano Lett.* **2013**, *13*, 3447–3454. [[CrossRef](#)] [[PubMed](#)]
4. Bernardi, M.; Palumbo, M.; Grossman, J.C. Extraordinary Sunlight Absorption and One Nanometer Thick Photovoltaics Using Two-Dimensional Monolayer Materials. *Nano Lett.* **2013**, *13*, 3664–3670. [[CrossRef](#)]
5. Jo, S.H.; Ubrig, N.; Berger, H.; Kuzmenko, A.B.; Morpurgo, A.F. Mono- and bilayer WS₂ light-emitting transistors. *Nano Lett.* **2014**, *14*, 2019–2025. [[CrossRef](#)]
6. Liang, L.; Meunier, V. First-principles Raman spectra of MoS₂, WS₂ and their heterostructures. *Nanoscale* **2014**, *21*, 5394–5401. [[CrossRef](#)]
7. Zibouche, N.; Kuc, A.; Heine, T. From layers to nanotubes: Transition metal disulfides TMS₂. *Eur. Phys. J. B* **2012**, *85*, 49. [[CrossRef](#)]
8. Kuc, A.; Zibouche, N.; Heine, T. Influence of quantum confinement on the electronic structure of the transition metal sulfide TS₂. *Phys. Rev. B* **2011**, *83*, 245213. [[CrossRef](#)]
9. Frey, G.L.; Tenne, R.; Matthews, M.J. Optical properties of MS₂ (M = Mo, W) inorganic fullerene like and nanotube material optical absorption and resonance Raman measurements. *J. Mater. Res.* **1998**, *13*, 9. [[CrossRef](#)]
10. Ghosh, S.; Brüser, V.; Kaplan, A.I.; Popovitz, B.R.; Peglow, S.; Martínez, J.I.; Alonso, J.A.; Zak, A. Cathodoluminescence in single and multiwall WS₂ nanotubes: Evidence for quantum confinement and strain effect. *Appl. Phys. Rev.* **2020**, *7*, 041401. [[CrossRef](#)]
11. Shanmugam, M.; Durcan, C.A.; Jacobs-Gedrim, R.; Yu, B. Layered semiconductor tungsten disulfide: Photoactive material in bulk heterojunction solar cells. *Nano Energy* **2013**, *2*, 419–424. [[CrossRef](#)]
12. Cheng, L.; Huang, W.; Gong, Q.; Liu, C.; Liu, Z.; Li, Y.; Dai, H. Ultrathin WS₂ Nanoflakes as a High-Performance Electrocatalyst for Hydrogen Evolution Reaction. *Angew. Chem. Int. Ed* **2014**, *53*, 7860–7863. [[CrossRef](#)] [[PubMed](#)]
13. Chen, T.Y.; Chang, Y.H.; Hsu, C.L.; Wei, K.H.; Chiang, C.Y.; Li, L.J. Comparative study on MoS₂ and WS₂ for electro-catalytic water splitting. *Hydrog. Energy Publ.* **2013**, *38*, 12302–12309. [[CrossRef](#)]
14. Feng, C.; Huang, L.; Guo, Z.; Liu, H. Synthesis of tungsten disulfide (WS₂) nanoflakes for lithium ion battery application. *Electrochem. Commun.* **2007**, *9*, 119. [[CrossRef](#)]
15. Huo, N.; Kang, J.; Wei, Z.; Li, S.S.; Li, J.; Wei, S.H. Novel and Enhanced Optoelectronic Performances of Multilayer MoS₂–WS₂ Heterostructure Transistors. *Adv. Funct. Mater* **2014**, *24*, 7025–7031. [[CrossRef](#)]
16. Elías, A.L.; Perea-López, N.; Castro-Beltrán, A.; Berkdemir, A.; Lv, R.; Feng, S.; Long, A.D.; Hayashi, T.; Kim, Y.A.; Endo, M.; et al. Controlled synthesis and transfer of large-area WS₂ sheets: From single layer to few layers. *ACS Nano* **2013**, *7*, 5235–5242. [[CrossRef](#)]
17. Miremadi, B.K.; Morrison, S.R. The intercalation and exfoliation of tungsten disulfide. *J. Appl. Phys.* **1988**, *63*, 4970–4974. [[CrossRef](#)]
18. Cong, C.; Shang, J.; Wu, X.; Cao, B.; Peimyoo, N.; Qiu, C.; Sun, L.; Yu, T. Synthesis and optical properties of large-area single-crystalline 2D semiconductor WS₂ monolayer from chemical vapor deposition. *Adv. Opt. Mater* **2013**, *2*, 131–136. [[CrossRef](#)]
19. Modtland, B.J.; Efrén, N.M.; Xiang, J.; Marc, B.; Jing, K. Monolayer tungsten disulfide (WS₂) via chlorine-driven chemical vapor transport. *Small* **2017**, *17*, 1701232. [[CrossRef](#)]
20. Wan, L.; Shi, C.W.; Yu, Z.B.; Wu, H.D.; Xiao, W.; Geng, Z.X.; Ren, T.Q.; Han, Q.; Yang, Z.X. Preparation of WS₂/C composite material and its electrocatalytic hydrogen evolution performance. *J. Fuel Chem. Technol.* **2021**, *49*, 1362–1370. [[CrossRef](#)]
21. Ramakrishna Matte, H.S.S.; Gomathi, A.; Manna, A.K.; Late, D.J.; Datta, R.; Pati, S.K.; Rao, C.N.R. MoS₂ and WS₂ Analogues of graphene. *Angew. Chem. Int. Ed* **2010**, *49*, 4059–4062. [[CrossRef](#)] [[PubMed](#)]
22. Schutte, W.J.; Deboer, J.L.; Jellinek, F. Crystal-Structures of Tungsten Disulfide and Diselenide. *J. Solid State Chem.* **1987**, *70*, 207–209. [[CrossRef](#)]
23. Prouzet, E.; Heising, J.; Kanatzidis, M.G. Structure of Restacked and Pillared WS₂: An X-ray Absorption Study. *Chem. Mater.* **2003**, *15*, 412–418. [[CrossRef](#)]
24. Wang, J.; Yu, L.; Zhou, Z.; Zeng, L.; Wei, M. Template-free synthesis of metallic WS₂ hollow microspheres as an anode for the sodium-ion battery. *J. Colloid Interface Sci.* **2013**, *557*, 722–728. [[CrossRef](#)] [[PubMed](#)]
25. Cao, H.; Wen, F.; De Hosson, J.T.M.; Pei, Y.T. Instant WS₂ platelets reorientation of self-adaptive WS₂/a-C tribocoating. *Mater. Lett.* **2018**, *229*, 64–67. [[CrossRef](#)]
26. Yang, W.; Wang, J.; Si, C.; Peng, Z.; Frenzel, J.; Eggeler, G.; Zhang, Z. [001] Preferentially-oriented 2D tungsten disulfide nanosheets as anode materials for superior lithium storage. *J. Mater. Chem A* **2015**, *3*, 17811. [[CrossRef](#)]
27. Xu, S.; Gao, X.; Hu, M.; Sun, J.; Wang, D.; Zhou, F.; Weng, L.; Liu, W. Morphology Evolution of Ag Alloyed WS₂ Films and the Significantly Enhanced Mechanical and Tribological Properties. *Surf. Coat. Technol.* **2014**, *238*, 197–206. [[CrossRef](#)]
28. Frey, G.L.; Elani, S.; Homyonfer, M.; Feldman, Y.; Tenne, R. Optical-absorption spectra of inorganic fullerene like MS₂ (M = Mo, W). *Phys. Rev. B* **1998**, *57*, 6666–6671. [[CrossRef](#)]

29. Beal, A.R.; Liang, W.Y. Excitons in 2H-WSe₂ and 3R-WS₂. *J. Phys. C Solid State Phys.* **1976**, *9*, 2459–2466. [[CrossRef](#)]
30. Berkdemir, A.; Gutiérrez, H.R.; Botello-Méndez, A.R.; Perea-López, N.; Elías, A.L.; Chia, C.I.; Wang, B.; Crespi, V.H.; López-Urías, F.; Charlier, J.C.; et al. Identification of individual and few layers of WS₂ using Raman Spectroscopy. *Sci. Rep.* **2013**, *3*, 1755. [[CrossRef](#)]
31. Zhao, W.; Ghorannevis, Z.; Amara, K.K.; Pang, J.R.; Toh, M.; Zhang, X.; Kloc, C.; Tan, P.H.; Eda, G. Lattice dynamics in mono- and few-layer sheets of WS₂ and WSe₂. *Nanoscale* **2013**, *5*, 9677. [[CrossRef](#)]
32. Tongay, S.; Zhou, J.; Ataca, C.; Lo, K.; Matthews, T.S.; Li, J.; Grossman, J.C.; Wu, J. Thermally Driven Crossover from Indirect toward Direct Bandgap in 2D Semiconductors: MoSe₂ versus MoS₂. *Nano Lett.* **2012**, *12*, 5576–5580. [[CrossRef](#)] [[PubMed](#)]
33. Lui, C.H.; Li, Z.; Chen, Z.; Klimov, P.V.; Brus, L.E.; Heinz, T.F. Imaging stacking order in few-layer graphene. *Nano Lett.* **2011**, *11*, 164–169. [[CrossRef](#)] [[PubMed](#)]
34. Stacy, A.M.; Hodul, D.T. Raman-Spectra of I_{vb} and V_{ib} Transition-Metal Disulfides Using Laser Energies near the Absorption Edges. *J. Phys. Chem. Solids* **1985**, *46*, 405–409. [[CrossRef](#)]
35. Molina-Sanchez, A.; Wirtz, L. Phonons in single-layer and few-layer MoS₂ and WS₂. *Phys. Rev. B* **2011**, *84*, 155413. [[CrossRef](#)]
36. Zhang, Y.; Zhang, Y.; Ji, Q.; Ju, J.; Yuan, H.; Shi, J.; Gao, T.; Ma, D.; Liu, M.; Chen, Y.; et al. Controlled Growth of High-Quality Monolayer WS₂ Layers on Sapphire and Imaging Its Grain Boundary. *ACS Nano* **2013**, *7*, 8963–8971. [[CrossRef](#)] [[PubMed](#)]
37. Huang, X.; Gao, Y.; Yang, T.; Ren, W.; Cheng, H.M.; Lai, T. Quantitative Analysis of Temperature Dependence of Raman shift of monolayer WS₂. *Sci. Rep.* **2016**, *6*, 32236. [[CrossRef](#)] [[PubMed](#)]
38. Song, J.G.; Park, J.; Lee, W.; Choi, T.; Jung, H.; Lee, C.W.; Hwang, S.H.; Myoung, J.M.; Jung, J.H.; Kim, S.H.; et al. Layer-Controlled, Wafer-Scale, and Conformal Synthesis of Tungsten Disulfide Nanosheets Using Atomic Layer Deposition. *ACS Nano* **2013**, *7*, 11333–11340. [[CrossRef](#)]
39. Sekine, T.; Nakashizu, T.; Toyoda, K.; Uchinokura, K.; Matsuura, E. Raman scattering in layered compound 2H-WS₂. *Solid State Commun.* **1980**, *35*, 371–373. [[CrossRef](#)]
40. Sie, E.J.; Steinhoff, A.; Gies, C.; Lui, C.H.; Ma, Q.; Rosner, M.; Schönhoff, G.; Jahnke, F.; Wehling, T.O.; Lee, Y.H.; et al. Observation of exciton redshift–blueshift crossover in monolayer WS₂. *Nano Lett.* **2017**, *14*, 4210–4216. [[CrossRef](#)]
41. Cao, S.; Zhao, C.; Han, T.; Peng, L. The WO₃/WS₂ nanostructures: Preparation, characterization and optical absorption properties. *Physical E* **2016**, *81*, 235–239. [[CrossRef](#)]
42. Sun, Y.; Darling, A.J.; Li, Y.; Fujisawa, K.; Holder, C.F.; Liu, H.; Janik, M.J.; Terrones, M.; Schaak, R.E. De-fect-mediated selective hydrogenation of nitroarenes on nanostructured WS₂. *Chem. Sci.* **2019**, *10*, 10310. [[CrossRef](#)] [[PubMed](#)]

Disclaimer/Publisher’s Note: The statements, opinions and data contained in all publications are solely those of the individual author(s) and contributor(s) and not of MDPI and/or the editor(s). MDPI and/or the editor(s) disclaim responsibility for any injury to people or property resulting from any ideas, methods, instructions or products referred to in the content.